Carrier Transport in Cubic Boron Nitride: First-Principles and Semiempirical Models

M. Zhu[1,*] M. Matsubara[1] and E. Bellotti[1,2]

[1]*ECE, Boston University, 8 Saint Mary's Street, Boston, Massachusetts 02215, USA*
[2]*Material Science Division, Boston University, 8 Saint Mary's Street, Boston, Massachusetts 02215, USA*

We perform a study of the transport properties of cubic boron nitride at low to high electric fields based on calculations performed by density-functional theory and full-band ensemble Monte Carlo. The full band structure and the carrier-phonon scattering rates are computed from first principles using density-functional theory with a hybrid functional and density-functional perturbation theory, respectively. The results of these calculations are used in an ensemble Monte Carlo simulator to calculate the velocities, energies, and impact ionization coefficients in different crystallographic directions. In conjunction, we have also developed the form-factor parameters to recreate the full band structure based on the empirical pseudopotential method, which is less computationally expensive and more accessible. The results of the transport calculations performed using the two differently computed band structures are compared.

I. INTRODUCTION

Ultrawide-band-gap (UWBG) semiconductors are classified as materials with band gaps greater than 4 eV. These materials are especially attractive to power electronics applications due to their high breakdown voltages and high operating temperatures, which are directly attributed to their wide band gaps [1,2]. Owing to these properties, power devices based on UWBG semiconductors are expected to outperform their counterparts based on wide-band-gap and more traditional semiconductors. The continued development of UWBG semiconductors also benefits ultraviolet (UV) optoelectronics, including light-emitting diodes and photodetectors, due to the closer match between their band gap and the desired photon energies.

Currently, UWBG semiconductors are considered an immature technology [1–3], with challenges including unreliable doping, poor material quality, and scalability affecting all UWBG materials. The $Al_xGa_{1-x}N$ alloy system, with a tunable band gap ranging from 3.4 eV to over 6 eV, and a breakdown field up to 10 MV cm^{-1}, can be considered the most technologically mature, and has already shown promise as a material for optoelectronics and power switching devices [1,3,4]. However, challenges with p-type doping and available substrates continue to be key areas of focus for the development of $Al_xGa_{1-x}N$ devices. Diamond has also been a material of interest owing to its large band gap of 5.5 eV, extremely high thermal conductivity, high carrier mobilities, similar breakdown fields,

and similar high-field velocities compared to $Al_xGa_{1-x}N$ [1,5–8]. So far, some progress has been made towards fabrication of diamond-based devices [9]. Nevertheless, the technology is still in its early stages and suffers from unreliable doping and material growth challenges.

In addition to the aforementioned UWBG materials, cubic boron nitride (c-BN) has also received some attention due to its superior material properties, similar to diamond, including high thermal conductivity and an even wider band gap of 6.4 eV [1,6]. This has inspired some work into the doping and growth of c-BN films [10–15], and the fabrication of rudimentary diodes [16]. However, little is known about its electrical transport properties. Sparse data exist on the transport properties at low fields below 10 kV cm^{-1}, both theoretically [17–19] and experimentally [20,21], with an estimated electron mobility of nearly 1000 cm^2 V^{-1} s^{-1}. Even fewer data are available at high electric fields exceeding 1 MV cm^{-1}. Thus, detailed studies of high-field transport properties in c-BN are needed, with high-field velocities and impact ionization coefficients of utmost interest, to further inspire the continued research of this material.

The primary goal of this work is to perform a detailed investigation of the high-field transport characteristics of c-BN at 300 K using established methods. The important parameters include high-field drift velocities and ionization coefficients for both electrons and holes. The dearth of available experimental data for c-BN promotes the use of state-of-the-art *ab initio* methods based on density-functional theory (DFT) to compute its electronic band structure and its carrier-phonon scattering rates. Although

---

*mjzhu@bu.edu

these methods are well established, their computational complexity and the required access to the software means performing these calculations can be costly. Thus, we have also developed reduced-order and more accessible band-structure models based on the empirical pseudopotential (EPM) methods that can be used by other researchers to study the transport properties of *c*-BN. In order to validate the EPM model, its calculations are compared with those obtained using the *ab initio* DFT model.

II. TRANSPORT MODEL

Full-band Monte Carlo (FBMC) is a well-established method for studying the transport properties of semiconductors at high fields, and has been used extensively to calculate important parameters, such as drift velocities and impact ionization coefficients, for a wide range of materials [22–29]. This method requires the calculation of the materials' full band structure using semiempirical methods, such as EPM, or *ab initio* methods, such as DFT, as well as the implementation of energy-dependent scattering rates calculated analytically or through *ab initio* methods.

In this work, the Monte Carlo simulations are performed using the FBMC code developed at Boston University [30]. The full band structure of *c*-BN is computed using a state-of-the-art first-principles density-functional-theory method with Heyd-Scuseria-Ernzerhof (HSE) hybrid functionals. Using the DFT-computed band structure, the phonon scattering rates and dispersion for the given band structure are computed with density-functional perturbation theory (DFPT). Finally, the impact ionization rates, which are crucial for determining the breakdown fields, are computed using previously derived methods based on Fermi's "golden rule." This combination of the FBMC simulator with DFT-computed band structure and scattering rates gives a thorough treatment for the particle transport phenomena of intrinsic *c*-BN without the effects of impurities and defects. More details about the DFT and DFPT calculations are given in the following sections.

Complementing this work are the same calculations using the EPM-computed band structure. EPM is considered the method of choice for calculating band structures for FBMC simulations owing to its low computational cost [31]. Thus, development of an EPM band-structure model for *c*-BN would allow for more widespread studies of its transport properties and *c*-BN-based devices with FBMC methods. The quality of the EPM band structure is dependent on the availability of accurate experimental data and/or *ab initio* calculations to obtain a fit of the screened atomic potential. This presents issues for *c*-BN due to its lack of experimental data, but can be resolved by using parameters extracted from the *ab initio* DFT-HSE band-structure calculations.

A. Electronic band structure

The DFT-HSE electronic structure of *c*-BN was obtained using the QUANTUM ESPRESSO (QE) package [32,33]. The core-valence interaction is described by the SG15 optimized norm-conserving Vanderbilt (ONCV) pseudopotentials [34,35]. The HSE hybrid functional [36] with 33% amount of exact exchange gives 6.32 eV indirect energy gap, which agrees well with the experimental value of 6.36 eV [37]. Using an $8 \times 8 \times 8$ Γ-centered grid of **k**-points sampled in the first Brillouin zone (FBZ) with a cutoff energy of 80 Ry is sufficient to reach convergence of the total energy, with an error within 1 meV per atom.

The EPM electronic structure has been derived using a model already employed to study other wide-band-gap semiconductors and reported in Ref. [31]. Its parameters for the screened local atomic potential, which are given in Appendix A, were obtained by comparing the output band structure to the *ab initio* DFT-HSE band structure.

To perform the transport simulations in FBMC, the energies and wave functions obtained from DFT-HSE or EPM are sampled in the irreducible wedge (IW) of the FBZ. The volume of the IW is divided into cubic elements, with energies and wave functions sampled at each corner and once at each edge of the cube. This makes each cube a quadratic brick element for serendipitous interpolation of the energies and velocities [38]. In addition, cubes at or near valley minima are refined due to the inaccuracies with interpolation near those regions [23]. For *c*-BN, the refinements are placed around Γ and X to account for the valence-band maxima and the conduction-band minima, respectively. Each refined cubic element is subdivided into 216 smaller cubic elements with the same placement of **k**-points at the corners and edges. This step improves the accuracy of energy and velocity calculations at low to moderate electric fields. In total, 93 401 **k**-points are used the sample over the entire IW, with energies and wave functions computed at each.

Figure 1 presents and compares the *c*-BN band-structure energies computed by DFT-HSE and EPM. In this work, only the six lowest-energy conduction bands and the three highest-energy valence bands are included. The lowest-energy valence band is excluded as it is inconsequential for the simulations. Relevant parameters, including the effective masses, have been included in the Appendix B. For valence bands, the heavy-hole, light-hole, and spin-orbit bands, listed by decreasing effective mass, show good agreement between the EPM and DFT-HSE models, which is promising for accurate hole transport simulations using the EPM band structure. For conduction bands, the lowest-energy band shows good agreement between the two models, and begins to show significant differences starting at 5 eV above the conduction-band minima. The density of states (DOS) are plotted in Fig. 2, and show good agreement from the EPM band structure up to
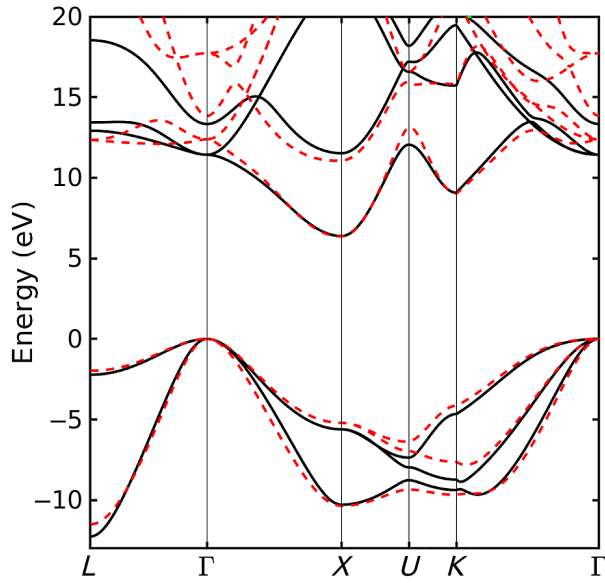
FIG. 1. Electronic band structure of cubic boron nitride computed using DFT-HSE (solid black lines) and local empirical pseudopotential method (dashed red lines).

5 eV for both the valence and conduction bands. These comparisons suggest that using the EPM band structure for FBMC transport calculations should yield accurate results as long as the particle energies do not exceed 5 eV.

B. Carrier-phonon scattering

The quantitative description of the carrier-phonon interaction is critical for the study of carrier dynamics at low and high electric fields. Conventional FBMC transport models incorporate scattering rates computed with simple models, using a deformation potential term as an empirical fitting parameter to scale acoustic and nonpolar scattering modes to match experimental data [25,28,39], such as mobility. However, this is not a viable option for c-BN, for which little or no experimental information is available, especially at high electric fields. Furthermore, since c-BN is a polar semiconductor, its mobility is expected to be less dependent on the deformation potential scattering, and more dependent on the long-range polar-optical modes. In this work, carrier-phonon scattering rates used in the FBMC calculations are computed using the conventional models, but are scaled with a deformation potential to match *ab-initio*-calculated scattering rates. For c-BN, it is important to include the deformation potential acoustic and nonpolar-optical phonons, as well as the polar-optical phonons. All rates are computed for a temperature of 300 K.

The *ab initio* scattering calculations start with the band structure computed from DFT-HSE combined with DFPT [40,41] to determine the phonon-resolved carrier-phonon scattering rate. This rigorous self-consistent approach
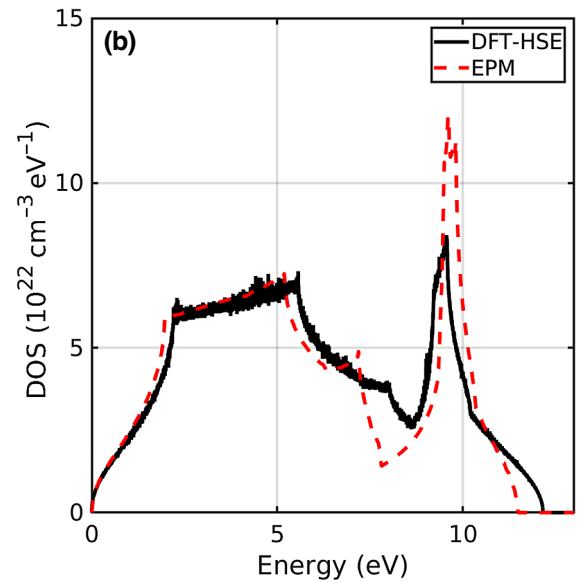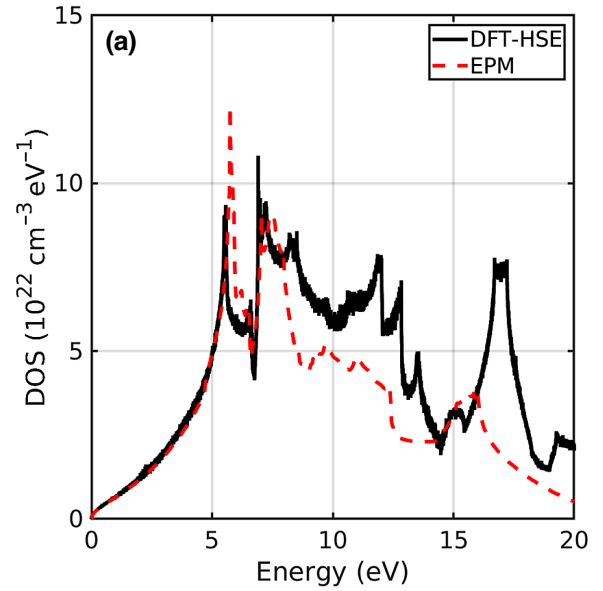

FIG. 2. Calculated conduction-band (top) and valence-band (bottom) density of states, computed using DFT-HSE (solid black line) and EPM (dashed red line).

includes the contribution of all phonon modes and accounts for the crystal potential variation resulting from the phonon mode propagation. The phonon dispersion is obtained within DFPT implemented in the QE package with an $8 \times 8 \times 8$ grid of phonon **q**-vectors using Perdew-Burke-Ernzerhof (PBE) functionals [42]. Figure 3 presents the calculated phonon dispersion in c-BN. Subsequently, the electron-phonon matrix elements and phonon-mode-resolved scattering rates are computed on a dense $80 \times 80 \times 80$ **k**-point and **q**-vector grids in the FBZ, using electron-phonon Wannier (EPW) software [43,44] through

maximally localized Wannier functions (MLWFs) [45] and generalized Fourier interpolation [46].

Although the *ab initio* approach provides the most rigorous calculation of the carrier-phonon scattering rates, it is difficult to implement the rates directly into FBMC simulations. Thus, the rates incorporated into FBMC are

computed using the following equations originally derived from Fermi's "golden rule" for the acoustic (ac) [22], nonpolar-optical (op) [22], and polar-optical (po) [43] absorption and emission processes, and requires integrating for each initial **k**-point, **k**, in each initial band, n, to each final **k**-point, **k**′, in each final band, n':

$$\frac{1}{\tau_{\mathrm{ac}}^{\pm}(n,\mathbf{k})} = \frac{2\pi}{\hbar} \sum_{n'} \int_V d\mathbf{k}' \frac{|\mathbf{q}|\pi (D_{\mathrm{ac}}(E))^2}{V\rho\omega_{\mathrm{ac}}} \left\{ N_q + \frac{1}{2} \pm \frac{1}{2} \right\} |I(n,\mathbf{k},n',\mathbf{k}')|^2 \times \delta[E(\mathbf{k}') - E(\mathbf{k}) \mp \hbar\omega_{\mathrm{ac}}(\mathbf{q})], \qquad (1)$$

$$\frac{1}{\tau_{\mathrm{op}}^{\pm}(n,\mathbf{k})} = \frac{2\pi}{\hbar} \sum_{n'} \int_V d\mathbf{k}' \frac{\pi (D_{\mathrm{t}}K(E))^2}{V\rho\omega_{\mathrm{op}}} \left\{ N_q + \frac{1}{2} \pm \frac{1}{2} \right\} |I(n,\mathbf{k},n',\mathbf{k}')|^2 \times \delta[E(\mathbf{k}') - E(\mathbf{k}) \mp \hbar\omega_{\mathrm{op}}(\mathbf{q})], \qquad (2)$$

$$\frac{1}{\tau_{\mathrm{po}}^{\pm}(n,\mathbf{k})} = \frac{2\pi}{\hbar} \sum_{n'} \int_V d\mathbf{k}' \frac{e^2 \hbar\omega_{\mathrm{lo}}}{4|\mathbf{q}|^2} \left[\frac{1}{\varepsilon_\infty} - \frac{1}{\varepsilon_0} \right] \left\{ N_q + \frac{1}{2} \pm \frac{1}{2} \right\} |I(n,\mathbf{k},n',\mathbf{k}')|^2 \times \delta[E(\mathbf{k}') - E(\mathbf{k}) \mp \hbar\omega_{\mathrm{lo}}(\mathbf{q})]. \qquad (3)$$

In these equations, e is the electronic charge, **q** is the phonon wave vector, N_q is the phonon number, ω and $\hbar\omega$ are the phonon angular frequency and phonon energy, respectively, ρ is the density of c-BN, ε_0 and ε_∞ are the low-frequency and high-frequency permittivity of c-BN, respectively, and $I(n,\mathbf{k},n',\mathbf{k}')$ is the overlap integral between corresponding Bloch wave functions. For momentum conservation, the condition $\mathbf{k}' = T_{\mathrm{FBZ}}(\mathbf{k} + \mathbf{q})$ needs to be satisfied, where $T_{\mathrm{FBZ}}(\mathbf{k} + \mathbf{q})$ stands for

the transformation of the **k**-vector, $\mathbf{k} + \mathbf{q}$, into the FBZ. The term $D_{\mathrm{ac}}(E)$ is the energy-dependent acoustic-phonon deformation potential, and $D_{\mathrm{t}}K(E)$ the energy-dependent nonpolar-optical-phonon deformation potential. In these equations, $N_q + \frac{1}{2} + \frac{1}{2}$ is used for absorption processes, and $N_q + \frac{1}{2} - \frac{1}{2}$ is used for emission processes. The Umklapp scattering processes are also included in the calculations. Relevant material parameters and constants are located in Appendix C.

The calculations of the scattering rates are performed using the DFT-HSE and EPM band structures sampled in the irreducible wedge with 93 401 **k**-points previously mentioned as the initial **k**-points. An additional mesh sampled in the entire FBZ is used as the final **k**-points and includes added mesh refinements placed at Γ and the six X points for a total of 492 141 **k**-points with only energies computed and 96 304 **k**-points with only wave functions computed placed as the center of the cubic elements.

The acoustic, nonpolar-optical, and polar-optical phonon branches are grouped to form *effective* modes for each, with the *effective* dispersions plotted on top of the *ab-initio*-calculated values in Fig. 3. The initially **k**-dependent scattering rates computed using Eqs. (1)–(3) are converted to energy-dependent rates using the $E(\mathbf{k})$ relation of the band structure. This method has been widely adopted in FBMC simulations [24–27] for its simplicity and effectiveness. The *effective* acoustic dispersion is isotropic with the phonon **q**-vector and the *effective* optical modes are represented by a single phonon energy of 127 meV for the
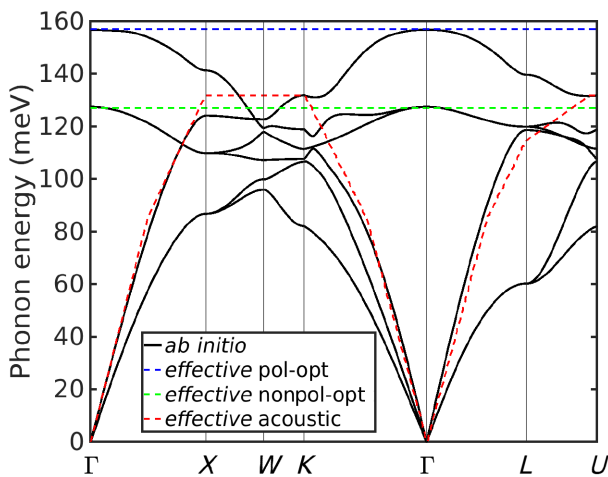

FIG. 3. *Ab-initio*-calculated phonon dispersion (solid lines) and the *effective* dispersion (dotted lines) for c-BN used in the FBMC calculations.

nonpolar-optical mode, and 157 meV for the polar-optical mode for all phonon **q**-vectors. It is important to distinguish between the two polar modes due to their difference in calculated scattering rates, as seen in Eqs. (2) and (3), and the differences in the final **k**-point selection process of the two modes. For example, scattering by a polar-optical phonon is much more likely to result in a final **k**-point closer to the initial **k**-point due to its $1/|\mathbf{q}|^2$ relation.

The final step in incorporating the scattering processes into the FBMC simulations is to scale the *effective* acoustic rates and the *effective* nonpolar-optical rates by the acoustic deformation potential, $D_{ac}(E)$, and the nonpolar-optical deformation potential, $D_t K(E)$, respectively, to match the corresponding *ab-initio*-computed rates. The results of the fitting process are shown in Figs. 4 and 5. The discrepancy between the shapes of the scattering rates computed using the EPM band structure *versus* using the DFT-HSE band structure can be immediately seen, with the biggest differences occurring above 5 V. This is mainly attributed to the differences in the DOS between the differently computed band structures. It is interesting to note that the hole *effective* acoustic scattering rate with both DFT-HSE and EPM data differ from the *ab-initio*-computed rate at low energies below 1.2 eV. This discrepancy stems from the rate calculated for the longitudinal acoustic-phonon branch, where the symmetry of the matrix elements is not properly accounted for in the *effective* model.

C. Impact ionization rates

The impact ionization process refers to the generation of electron-hole pairs due to scattering between a high-energy electron (or hole) with an electron in the valence band. This process is especially important to include in high-field simulations since it is responsible for breakdown, which limits the operating regime of high-voltage devices, such as power devices.

The impact ionization (ii) scattering rates are computed to the first order using previously derived methods based on Fermi's "golden rule" [24,25,47–49]. In this process, an initiating electron or hole with **k**-vector, $\mathbf{k}_1$, in band n_1 ionizes with a bound electron in the valence band with $\mathbf{k}_2$ in band n_2. The initiating electron or hole is scattered to its final state with $\mathbf{k}_{1'}$ in the conduction or valence band $n_{1'}$, respectively. The bound electron is scattered into the conduction band with $\mathbf{k}_{2'}$ in band $n_{2'}$, leaving behind a hole with $\mathbf{k}_2$ in the valence band n_2. The equation for this process is

$$\frac{1}{\tau_{ii}(n,\mathbf{k}_1)} = \frac{2\pi}{\hbar} \frac{V^3}{(2\pi)^9} \sum_{n_{1'},n_2,n_{2'}} \iiint d\mathbf{k}_{1'}\, d\mathbf{k}_2\, d\mathbf{k}_{2'}$$

$$|M(n_{1'}\mathbf{k}_{1'}, n_{2'}\mathbf{k}_{2'}; n_1\mathbf{k}_1, n_2\mathbf{k}_2)|^2$$

$$\times \delta[E(\mathbf{k}_1) + E(\mathbf{k}_{1'}) - E(\mathbf{k}_2) - E(\mathbf{k}_{2'})], \quad (4)$$
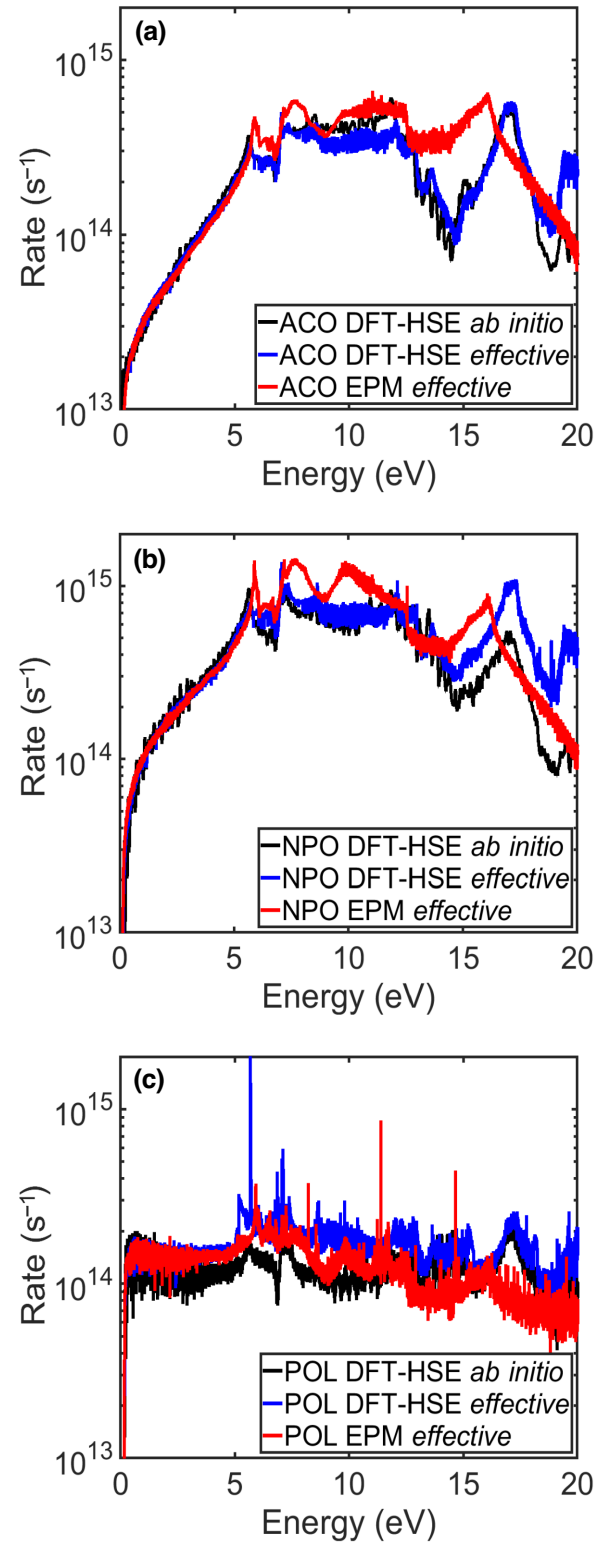

FIG. 4. Comparison between electron acoustic (ACO), nonpolar-optical (NPO), and polar-optical (POL) scattering rates of the *ab initio* DFT-HSE computed rates to their equivalent *effective* scattering rates. Deformation potentials are applied to the *effective* acoustic (top) and *effective* nonpolar-optical modes (middle). No deformation potential is applied to the polar-optical scattering rates (bottom).
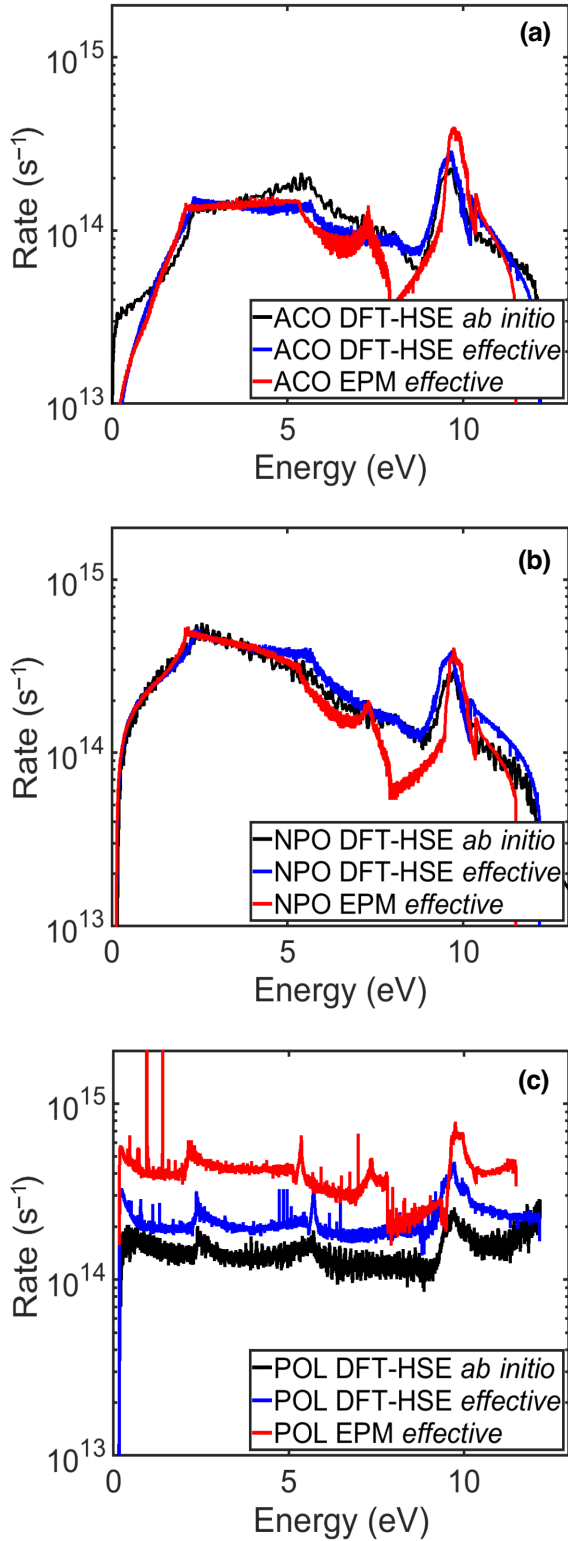
FIG. 5. Comparison between hole acoustic (ACO), nonpolar-optical (NPO), and polar-optical (POL) scattering rates of the *ab initio* DFT-HSE computed rates to their equivalent *effective* scattering rates. Deformation potentials are applied to the *effective acoustic* (top) and *effective nonpolar-optical* modes (middle). No deformation potential is applied to the polar-optical scattering rates (bottom).
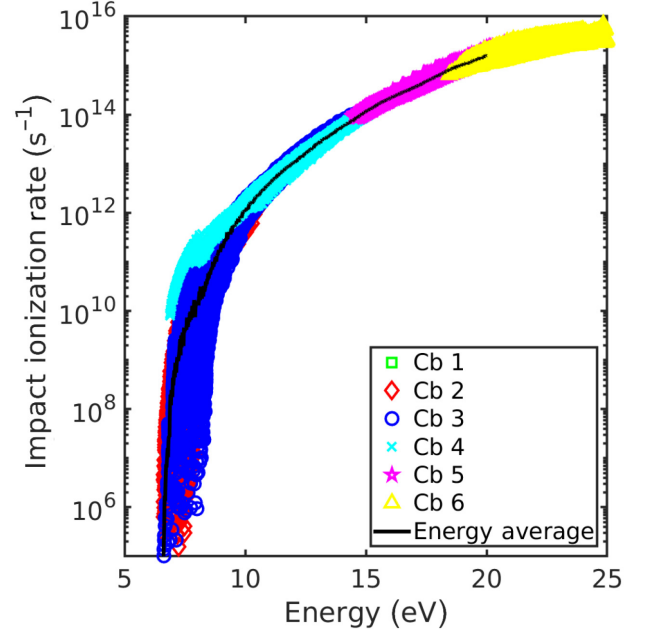

FIG. 6. Electron-initiated impact ionization transition rate evaluated using the electronic structure from DFT-HSE.

where M is the screened Coulomb matrix element, and the **k**-vectors are restricted to lie in the FBZ and to satisfy momentum conservation, $\mathbf{k}_1 + \mathbf{k}_2 + \mathbf{G}_U = \mathbf{k}_{1'} + \mathbf{k}_{2'}$, where $\mathbf{G}_U$ is a reciprocal lattice vector.

With particles treated as being indistinguishable, the matrix element for the ionization transition consists of the direct, M_D, and exchange, M_E, processes: $|M|^2 = |M_D|^2 + |M_E|^2 - (M_D^* M_E + M_D M_E^*)/2$. The direct matrix element may be computed as [24,49]

$$
\begin{aligned}
M_D = &\sum_{\mathbf{G}_1, \mathbf{G}_2, \mathbf{G}_{1'}, \mathbf{G}_{2'}} a_{n_{1'}\mathbf{k}_{1'}}^*(\mathbf{G}_{1'}) a_{n_{2'}\mathbf{k}_{2'}}^*(\mathbf{G}_{2'}) a_{n_1\mathbf{k}_1}(\mathbf{G}_1) a_{n_2\mathbf{k}_2} \\
&\times (\mathbf{G}_2) \frac{e^2}{4\pi\epsilon(\mathbf{q}_D, \omega_D) q_D^2} \delta(-\mathbf{k}_{1'} - \mathbf{G}_{1'} + \mathbf{k}_1 + \mathbf{G}_1 \\
&- \mathbf{k}_{2'} - \mathbf{G}_{2'} + \mathbf{k}_2 + \mathbf{G}_2),
\end{aligned}
\tag{5}
$$

where $\hbar\omega_D = E(\mathbf{k}_1) - E(\mathbf{k}_{1'})$ and $\mathbf{q}_D = \mathbf{k}_{1'} + \mathbf{G}_{1'} - \mathbf{k}_1 - \mathbf{G}_1$ are the direct energy and momentum transfer, respectively. The exchange term M_E is obtained by simply exchanging the final states $(1', 2') \rightarrow (2', 1')$ in Eq. (5). The major difficulty in the evaluation of impact ionization matrix elements M_D and M_E lies in choosing an accurate yet manageable expression for the dielectric matrix. In this work, the valence-band contribution to the dielectric function has been computed within the random-phase approximation (RPA) [50]. The results of these calculations using the DFT-HSE band structure are presented in Figs. 6 and 7.
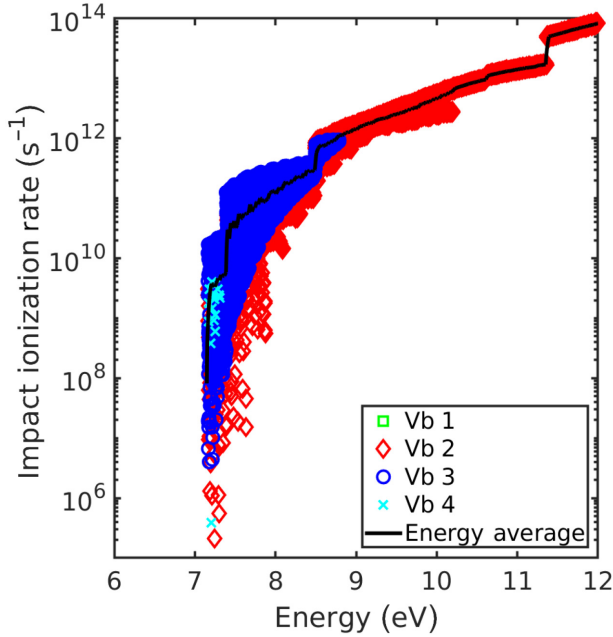
FIG. 7. Hole-initiated impact ionization transition rate evaluated using the electronic structure from DFT-HSE.

FIG. 8. Electron and hole drift velocities evaluated using the electronic structure and scattering rates from DFT-HSE and EPM.

III. RESULTS AND DISCUSSION

Using the approach outlined in Sec. II, the carrier drift velocities and average energies at 300 K are computed with FBMC for electric fields ranging from 500 V cm^{-1} to 10 MV cm^{-1} in the crystallographic directions $\langle 100 \rangle$, $\langle 110 \rangle$, and $\langle 111 \rangle$. The impact ionization coefficients have also been computed for both electrons and holes for the same electric field strengths and directions. Using the computed ionization coefficients, the estimated breakdown field for c-BN is acquired from one-dimensional (1D) FBMC device simulations. The key carrier transport parameters for c-BN computed with FBMC in this work are compared to other UWBG semiconductors in Table I. The wide range of reported breakdown fields likely comes from differences in device design, such as doping concentration, channel length, and edge termination [54].
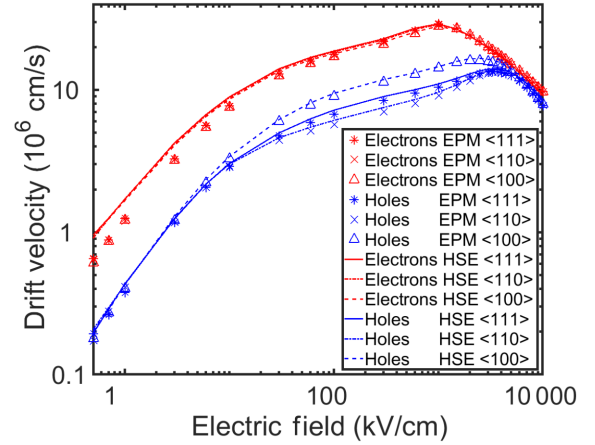
A. Drift velocities

The FBMC-calculated drift velocities for c-BN computed using the DFT-HSE and EPM band structures are shown in Fig. 8. FBMC simulations start with seeding an ensemble of electrons or holes in an electric field, which are accelerated by the field and scattered according to their energy. The carrier drift velocities are defined as the average velocity of the ensemble in the direction of the electric field at steady state. The velocity of each carrier is calculated as $\partial E / \partial \mathbf{k}$, where E and $\mathbf{k}$ are the carriers' energy and $\mathbf{k}$-vector, respectively. The calculations show that electron velocities are isotropic for all simulated field strengths, with a peak velocity of 2.7×10^7 cm s^{-1} occurring at a field of 1 MV cm^{-1}. This value is comparable to or slightly higher than the electron peak velocity in diamond, and significantly higher than reported values in Al$_x$Ga$_{1-x}$N. The estimated intrinsic electron mobility, estimated from the linear slope of the velocity curve at low fields, is 1600 cm^2 V^{-1} s^{-1} and is comparable to previously computed values [17,19], but higher than the measured values [20].

TABLE I. Comparison of electron and hole mobilities (if available), μ_e and μ_h, maximum drift velocities, $v_{\max,e}$ and $v_{\max,h}$, and the breakdown field, $F_{\text{breakdown}}$, between c-BN computed in this work with Al$_x$Ga$_{1-x}$N [1,2,4,51,52] and diamond [1,5,7,8,53]. The breakdown field provided for c-BN represents devices with a channel length of 10 μm or shorter.

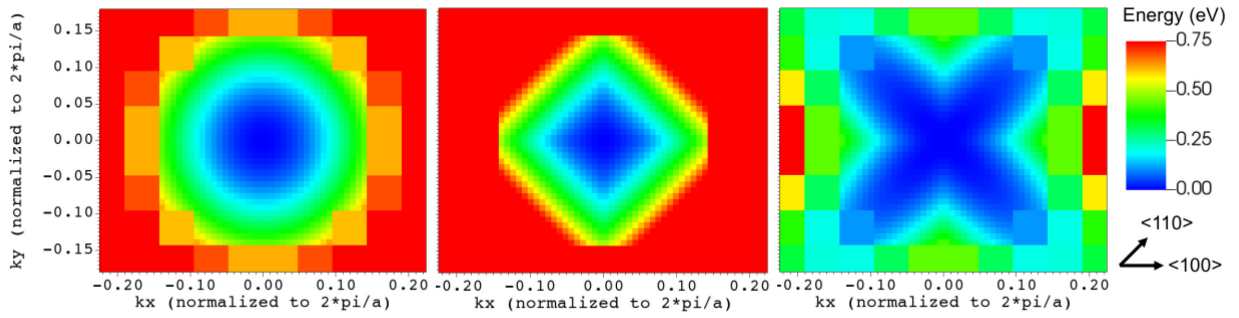| Material	μ_e μ_h (cm^2 V^{-1} s^{-1})	$v_{\max,e}$ $v_{\max,h}$ (cm s^{-1})	$F_{\text{breakdown}}$ (MV cm^{-1})
c-BN	1600	2.7×10^7	> 5.5
(this work)	400	1.6×10^7	
Diamond	2500	2.5×10^7	2–20
	2200	1×10^7	
Al$_x$Ga$_{1-x}$N	450	1.5×10^7	1–10
	$\cdots$	$\cdots$	

FIG. 9. Two-dimensional cross section along the k_z plane of the FBZ of the energy dispersion for the top three valence bands centered at Γ for c-BN computed by HSE. A high degree of anisotropy is observed in the heavy-hole band (right panel). Some anisotropy is observed in the light-hole band (middle panel), and no anisotropy is observed in the spin-orbit band (left panel). The increased resolution surrounding Γ comes from mesh refinements placed in this region. This figure was generated using VisIt [55].

Unlike electrons, holes exhibit significant anisotropy that is observed in the range between 10 and 4 MV cm^{-1}. The $\langle 100 \rangle$ crystallographic direction reaches the highest velocities, with a peak velocity of 1.6×10^7 cm s^{-1} for an applied field of 2.5 MV cm^{-1}. The peak velocity value is higher than the reported hole peak velocity in diamond. The anisotropy can be largely attributed to the anisotropic effective masses of the heavy-hole valence band that can be seen in Fig. 1 and more clearly presented in Fig. 9, and shows the much higher effective mass in the $\langle 110 \rangle$ direction compared to the $\langle 100 \rangle$ direction. This anisotropy disappears for fields greater than 4.0 MV cm^{-1}. Using the slope of the hole velocity at low fields, the hole mobility is estimated to be 400 cm^2 V^{-1} s^{-1} and matches well with previously measured results [56].

A comparison of the FBMC velocity results calculated with DFT-HSE and EPM band structures and scattering rates shows no significant differences. For the simulations up to 10 MV cm^{-1}, the average energies for both electrons and holes do not exceed 5 eV, as shown in Fig. 10. Since the DFT-HSE and EPM band structures only begin to show significant differences starting at 5 eV, as seen in the band structure in Fig. 1 and the DOS in Fig. 2, the EPM band structure serves as a satisfactory alternative for FBMC simulations of carrier velocities for fields up to 10 MV cm^{-1} and possibly higher.

B. Ionization coefficients and breakdown field

Impact ionization coefficients are crucial for modeling of power devices and the prediction of their breakdown voltage. For optoelectronic devices, impact ionization coefficients can be used to estimate their gain and noise characteristics. The electron-initiated, α, and hole-initiated, β, ionization coefficients, defined as the inverse mean free path between ionization events, have been extracted along the principal crystallographic directions for applied electric field strengths up to 10 MV cm^{-1}.

It is important to discern between the ionization *coefficient* discussed in this section, which has units of cm^{-1}, and the ionization *rate*, with units of s^{-1}, discussed in Sec. II C. Figure 11 presents the calculated values for α and β using the DFT-HSE and EPM band structures, and shows that holes are the dominant ionizers in c-BN for the sampled electric field strengths. Compared to previously computed ionization coefficients of diamond [29,54,57], for which holes also dominate the ionization process up to 10 MV cm^{-1}, c-BN has much lower coefficients, which is likely attributed to its wider band gap. For example, the calculated β of c-BN for an electric field strength of 5 MV cm^{-1} is 5×10^3 cm^{-1}, compared to calculated values of $\approx 1 \times 10^4$ cm^{-1} to $\approx 1 \times 10^5$ cm^{-1} and higher in diamond. This is a promising sign that c-BN may have a higher breakdown field compared to diamond.

To obtain preliminary estimates of the breakdown fields in c-BN, 1D FBMC device simulations are performed on c-BN p-i-n diodes. The intrinsic region serves as the channel,
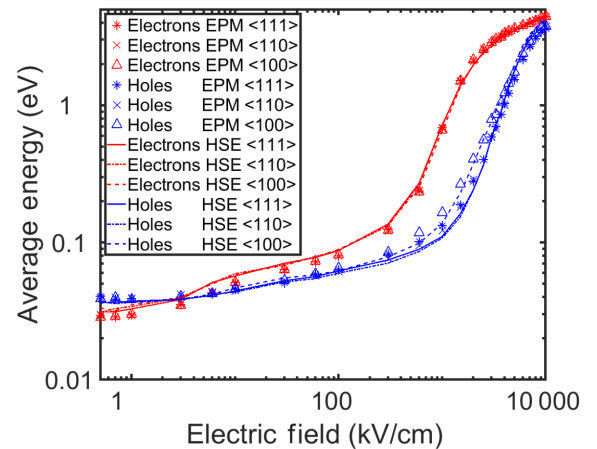

FIG. 10. Electron and hole average energies evaluated using the electronic structure and scattering rates from EPM and DFT-HSE.
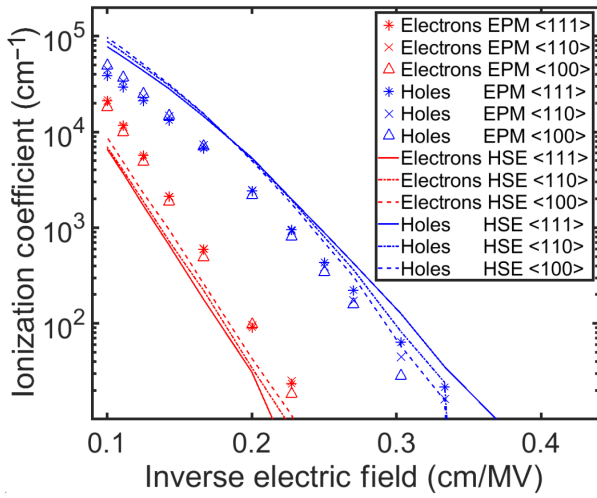
FIG. 11. Calculated electron and hole ionization coefficients for different crystallographic directions and using the electronic structure and scattering rates from DFT-HSE and EPM.

FIG. 12. Calculated electric field profile of a 1D *p-i-n* diode used to estimate the breakdown field. The intrinsic region width is 5 μm. Contacts are located at the extremes of the device. As the bias is increased, the electric field will also increase but maintain its uniformity.

with lengths of 1, 5, and 10 μm, and doped at a concentration of 1×10^{13} cm^{-3}. The low doping concentration creates uniform electric fields along the channel, which are useful for estimating their breakdown field. Sample electric field profiles for the 5 μm channel are presented in Fig. 12. The simulations start with the injection of holes at the *n* side of the *p-i-n* diode, which are then accelerated towards the *p* side, gain energy through the field, and undergo impact ionizations. Holes are injected instead of electrons since they have the higher ionization coefficient and a higher probability of triggering breakdown. The current gain, M, for each electric field value is computed as $(N_{\text{ion}}/N_{\text{injected}}) + 1$, where N_{ion} is the number of ionization events that occurred and N_{injected} is the number of holes injected. For this study, the breakdown field is defined as the electric field for which the gain exceeds 1×10^{6} A/A.

The results of this study are presented in Fig. 13, and show that, for the longest device with a 10 μm channel, breakdown occurs for a field of 5.5 MV cm^{-1}. For the 5 μm channel, the breakdown field is increased to 6.5 MV cm^{-1}, and for the 1 μm channel, breakdown was not observed up to 10 MV cm^{-1}. These breakdown fields fall within the range of experimental values reported for diamond and Al$_x$Ga$_{1-x}$N. The observed trend of higher breakdown fields for shorter channels can be explained by ionization deadspace [58]. In other words, low-energy carriers, which include the initially seeded carriers and the carriers generated from impact ionization events, must travel a finite distance before gaining enough energy to impact-ionize. Thus, longer channels will incur a higher number of ionizations for a given set of ionization coefficients. Based on this trend, it is likely that the breakdown field can go well beyond 10 MV cm^{-1} for channel lengths shorter than 1 μm. Furthermore, it should be noted that the
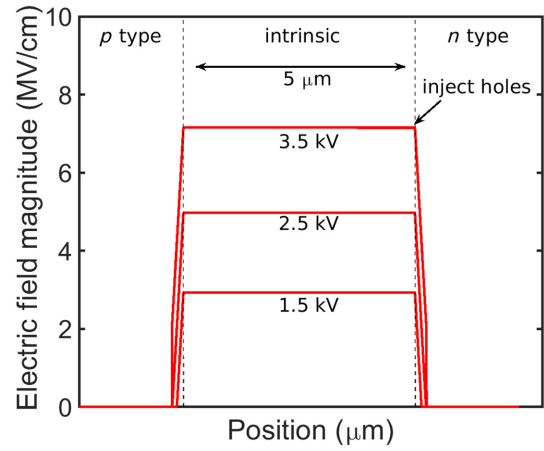
doping level of the high-electric-field region significantly affects the breakdown field for real devices, with higher doping levels resulting in higher breakdown fields [54]. Thus, it is likely the calculated 5.5 MV cm^{-1} breakdown field for the 10 μm channel represents the lower-bound estimate for devices with a channel shorter than 10 μm.

Lastly, differences between the extracted ionization coefficients obtained using the DFT-HSE and EPM band structures are compared. The discrepancy between the set of coefficients can be traced to the differences in the DOS of the two band structures. Impact ionizations occur at the extremes of the energy distribution well above 5 eV
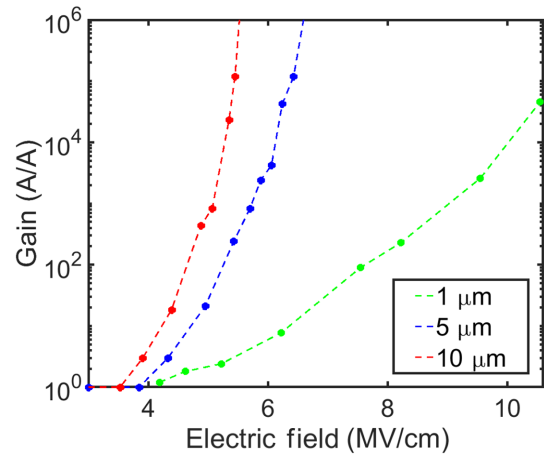

FIG. 13. FBMC-simulated gain of an injected hole in a *c*-BN *p-i-n* diode. Breakdown is defined as a gain exceeding 1×10^{6} A/A. Breakdown occurs at 5.5 MV cm^{-1} for the 10 μm device, and at 6.5 MV cm^{-1} for the 5 μm device. Breakdown was not observed for the 1 μm device.
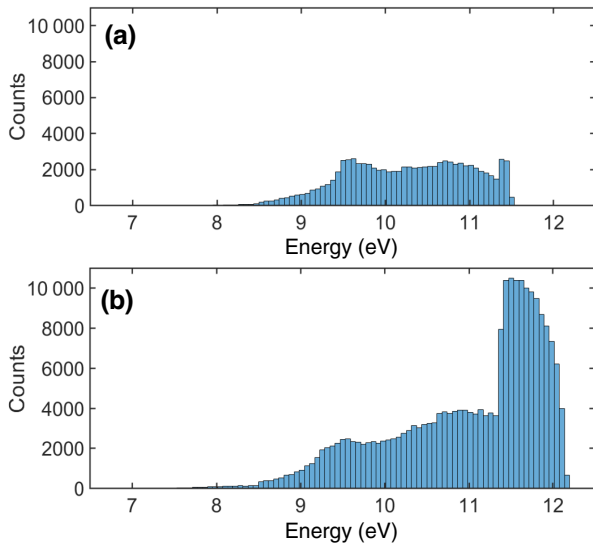
FIG. 14. Histogram of energies for which the ionization events occur, comparing results from EPM bands (top) and HSE bands (bottom).

for both electrons and holes, where the DFT-HSE and EPM band structures show significant differences. The histogram of hole ionizations for 10 MV cm^{-1} in the $\langle 100 \rangle$ direction is presented in Fig. 14 and shows that hole ionizations start to occur for hole energies of 8 eV, and the number of ionizations starts to drastically increase at 11.3 eV. Since the DOS of the EPM band structure approaches zero at a lower energy than the DFT-HSE band structure, the number of hole ionizations is higher for the DFT-HSE band structure.

IV. CONCLUSION

This work presents a numerical study of the carrier transport properties of cubic boron nitride using *ab-initio*-calculated band structure and scattering rates. The band structure was computed using a first-principles model based on density-functional theory, and the carrier-phonon scattering rates were evaluated using density-functional perturbation theory. In addition, we have also developed a low-computational-cost band structure based on an empirical pseudopotential. These models are applied to full-band Monte Carlo simulations of cubic boron nitride to extract its carrier transport properties, including carrier velocities at high field and impact ionization coefficients.

The results of the full-band Monte Carlo simulations show a peak electron velocity of 2.7×10^7 cm s^{-1} at an applied field strength of 1.0 MV cm^{-1}, and a peak hole velocity of 1.6×10^7 cm s^{-1} at an applied field of 2.5 MV cm^{-1} in the $\langle 100 \rangle$ direction. For holes, anisotropy is observed for electric fields ranging from 10 kV cm^{-1} to 4.0 MV cm^{-1}, with drift velocities approximately 1.5 times

lower in the $\langle 110 \rangle$ and $\langle 111 \rangle$ directions. These velocity values for electrons and holes are comparable to or higher than the peak velocities of diamond and Al$_x$Ga$_{1-x}$N. The calculated carrier mobilities at 300 K are 1600 cm^2 V^{-1} s^{-1} for electrons and 400 cm^2 V^{-1} s^{-1} for holes, values that are lower than those of diamond but higher than those of Al$_x$Ga$_{1-x}$N. The high carrier velocities of cubic boron nitride at high electric fields are promising for its use in high-speed devices.

Impact ionization coefficients have also been extracted from the simulations, showing that holes have a much higher ionization coefficient than electrons. Compared to diamond, which has a relatively high breakdown field, the coefficients for cubic boron nitride appear to be lower than previously computed values of diamond, which is promising for even higher breakdown fields in cubic boron nitride. The estimated breakdown field from simulations of a simple *p-i-n* diode show a breakdown field of 5.5 MV cm^{-1} for a 10 μm channel, which falls within the range of reported breakdown fields of diamond and Al$_x$Ga$_{1-x}$N, and can be increased with shorter channel lengths.

Lastly, we have compared the carrier transport results using the band structures obtained from empirical pseudopotential and density-functional-theory methods and see that the calculations of mobility and high-field velocities yield similar values for all sampled electric fields up to 10 MV cm^{-1}. However, the calculated ionization coefficients show differences due to the differences between the band structures at high energies where the ionizations occur.

Based on the results of this study, *c*-BN is a material with transport properties that are favorable for high-speed power switches and high-frequency transistors.

APPENDIX A: EPM MODEL PARAMETERS

The EPM model for *c*-BN has been developed starting from the electronic structure computed using DFT-HSE. The local symmetric and antisymmetric form factors have been obtained using a spline interpolation and a cutoff has been introduced for $q^2 > 16$. The symmetric and

TABLE II. Form factors.

$V^{s,a}(q)$	Form factor (eV)
$V^s_{\sqrt{0}}$	−2.770682805958579
$V^s_{\sqrt{3}}$	−0.072685734490557
$V^s_{\sqrt{8}}$	0.573910302368103
$V^s_{\sqrt{11}}$	0.464990332323846
$V^a_{\sqrt{0}}$	−5.889089812295032
$V^a_{\sqrt{3}}$	0.690060172195140
$V^a_{\sqrt{4}}$	0.672669400807859
$V^a_{\sqrt{11}}$	0.356925317314253

antisymmetric form factors are given by Eq. (A1) [59,60]:

$$V^{s,a}(q) = V^{s,a}_{\text{spline}}(q) \times \frac{1}{2}\left[1 + \tanh\left(\frac{a_0 - q^2}{a_1}\right)\right], \quad (A1)$$

with $a_0 = 16.42$ and $a_1 = 0.8663$. Nonlocal correction and spin-orbit interaction have not been included in the model, and 113 plane waves have been used to represents the Bloch wave functions. Table II provides the values of the nonzero symmetric and antisymmetric form factors.

APPENDIX B: EFFECTIVE MASSES

The values of the effective masses at the conduction- and valence-band edges can also be used to compare the electronic band structures obtained from DFT-HSE and EPM. Because of the uncertainty introduced by evaluating numerically the second derivative of the energy with respect to the wave vector along specific crystallographic directions in the Brillouin zone, we have computed the effective masses by fitting the band-resolved DOS for the conduction, heavy, light, and split-orbit bands. Additionally we have computed the hole mass from the total valence DOS. Using the expression $g(E)$ of the DOS for a nonparabolic spherical band, reported in Eq. (B1) [61], we obtained the DOS mass m_d and the nonparabolicity coefficient α, fitting the analytical expression of the DOS to the numerically computed one from DFT-HSE and EPM, up

TABLE III. DOS-derived effective masses, m^*, and nonparabolicity factors, α, from DFT-HSE and EPM.

	DFT-HSE		EPM	
	m^*	α	m^*	α
Electrons	0.375	0.15	0.413	0.1
Holes, total	1.95	0.075	2.10	0.08
Heavy hole	1.10	0.00	1.15	0.025
Light hole	0.375	0.19	0.385	0.22
Spin-orbit	0.175	0.10	0.150	0.1

TABLE IV. Material parameters for c-BN at 300 K.

Relative permittivity, static	7.10
Relative permittivity, high-freq.	4.46
Lattice constants	3.62 Å
Density	3450 kg m^{-3}
Nonpolar-optical phonon energy	127 meV
Polar-optical phonon energy	157 meV

to 1 eV above the band edges:

$$g(E) = \frac{10^{-6}M^{2/3}m_d^{3/2}}{\sqrt{2}q^{3/2}\pi^2\hbar^3}(1 + 2\alpha E)\sqrt{E(1 + \alpha E)}, \quad (B1)$$

where M is the number of equivalent valleys, q is the electron charge in coulombs, and E the energy in electron volts.

Table III presents the DOS-derived masses and nonparabolicity coefficients for DFT-HSE and EPM. We can see that there is a good agreement between the two sets of effective masses. The differences in the values are probably within the fitting error. This result indicates that the EPM model reproduces well the DFT-HSE bands close to the band edges.

APPENDIX C: CUBIC BORON NITRIDE MATERIAL PARAMETERS

The material parameters for cubic boron nitride at 300 K used in this work are listed in Table IV.

[1] J. Tsao, S. Chowdhury, M. Hollis, D. Jena, N. Johnson, K. Jones, R. Kaplar, S. Rajan, C. Van de Walle, and E. Bellotti, *et al.*, Ultrawide-bandgap semiconductors: Research opportunities and challenges, Adv. Electron. Mater. **4,** 1600501 (2018).

[2] J. Yang, K. Liu, X. Chen, and D. Shen, Recent advances in optoelectronic and microelectronic devices based on ultrawide-bandgap semiconductors, Prog. Quantum Electron. **83,** 100397 (2022).

[3] M. H. Wong, O. Bierwagen, R. J. Kaplar, and H. Umezawa, Ultrawide-bandgap semiconductors: An overview, J. Mater. Res. **36,** 4601 (2021).

[4] P. Siddiqua, W. A. Hadi, M. S. Shur, and S. K. O'Leary, A 2015 perspective on the nature of the steady-state and transient electron transport within the wurtzite phases of gallium nitride, aluminum nitride, indium nitride, and zinc oxide: A critical and retrospective review, J. Mater. Sci.: Mater. Electron. **26,** 4475 (2015).

[5] N. Donato, N. Rouger, J. Pernot, G. Longobardi, and F. Udrea, Diamond power devices: State of the art, modelling, figures of merit and future perspective, J. Phys. D: Appl. Phys. **53,** 093001 (2019).

[6] A. Soltani, A. Talbi, V. Mortet, A. BenMoussa, W. Zhang, J.-C. Gerbedoen, J.-C. De Jaeger, A. Gokarna, K. Haenen, and P. Wagner, in *AIP Conference Proceedings*, Vol. 1292

(American Institute of Physics, Strasbourg, France, 2010), p. 191.

[7] M. Nesladek, A. Bogdan, W. Deferme, N. Tranchant, and P. Bergonzo, Charge transport in high mobility single crystal diamond, Diam. Relat. Mater. **17**, 1235 (2008).

[8] C. J. Wort and R. S. Balmer, Diamond as an electronic material, Mater. Today **11**, 22 (2008).

[9] K. G. Crawford, J. D. Weil, P. B. Shah, D. A. Ruzmetov, M. R. Neupane, K. Kingkeo, A. G. Birdwell, and T. G. Ivanov, Diamond field-effect transistors with V_2O_5-induced transfer doping: Scaling to 50-nm gate length, IEEE Trans. Electron Devices **67**, 2270 (2020).

[10] H. Yin, in *Gallium Nitride Materials and Devices XI*, Vol. 9748 (SPIE, 2016), p. 974805.

[11] D. F. Storm, S. I. Maximenko, A. C. Lang, N. Nepal, T. I. Feygelson, B. B. Pate, C. A. Affouda, and D. J. Meyer, Mg-facilitated growth of cubic boron nitride by ion beam-assisted molecular beam epitaxy, Phys. Status Solidi RRL **16**, 2200036 (2022).

[12] D. Kester, K. Ailey, D. Lichtenwalner, and R. Davis, Growth and characterization of cubic boron nitride thin films, J. Vac. Sci. Technol. A: Vac. Surf. Films **12**, 3074 (1994).

[13] L. Cai, B. Xu, M. Lv, F. Jia, and X. Yuan, Analysis of cubic boron nitride single crystal defects growth under high temperature and high pressure, J. Chem. **2020**, 1 (2020).

[14] K. Hirama, Y. Taniyasu, H. Yamamoto, and K. Kumakura, Control of n-type electrical conductivity for cubic boron nitride (c-BN) epitaxial layers by Si doping, Appl. Phys. Lett. **116**, 162104-1 (2020).

[15] T. Joshi, P. Kumar, B. Poudyal, S. P. Russell, P. Manchanda, and P. Dev, Doping limitations of cubic boron nitride: Effects of unintentional defects on shallow doping, Phys. Rev. B **105**, 054101 (2022).

[16] O. Mishima, J. Tanaka, S. Yamaoka, and O. Fukunaga, High-temperature cubic boron nitride pn junction diode made at high pressure, Science **238**, 181 (1987).

[17] N. Sanders and E. Kioupakis, Phonon- and defect-limited electron and hole mobility of diamond and cubic boron nitride: A critical comparison, Appl. Phys. Lett. **119**, 062101-1 (2021).

[18] P. Siddiqua, M. S. Shur, and S. K. O'Leary, Electron transport within bulk cubic boron nitride: A Monte Carlo simulation analysis, J. Appl. Phys. **128**, 185704-1 (2020).

[19] J. Chilleri, Y. Wang, M. S. Shur, and S. K. O'Leary, A low-field electron mobility analysis of cubic boron nitride, Solid State Commun. **352**, 114776 (2022).

[20] C.-X. Wang, G.-W. Yang, T.-C. Zhang, H.-W. Liu, Y.-H. Han, J.-F. Luo, C.-X. Gao, and G.-T. Zou, High-quality heterojunction between p-type diamond single-crystal film and n-type cubic boron nitride bulk single crystal, Appl. Phys. Lett. **83**, 4854 (2003).

[21] S. N. Mohammad, Electrical characteristics of thin film cubic boron nitride, Solid State Electron. **46**, 203 (2002).

[22] C. Jacoboni and P. Lugli, *The Monte Carlo Method for Semiconductor Device Simulation* (Springer, Vienna, Austria, 2012).

[23] K. Hess, *Monte Carlo Device Simulation: Full Band and Beyond* (Springer Science+Business Media New York City, USA, 2012), Vol. 144.

[24] F. Bertazzi, M. Moresco, and E. Bellotti, Theory of high field carrier transport and impact ionization in wurtzite GaN. Part I: A full band Monte Carlo model, J. Appl. Phys. **106**, 063718-1 (2009).

[25] M. V. Fischetti, N. Sano, S. Laux, and K. Natori, Full-band-structure theory of high-field transport and impact ionization of electrons and holes in Ge, Si, and GaAs, J. Technol. Comput.-Aided Des. TCAD **1** (1996).

[26] M. Hjelm, H.-E. Nilsson, A. Martinez, K. Brennan, and E. Bellotti, Monte Carlo study of high-field carrier transport in 4H-SiC including band-to-band tunneling, J. Appl. Phys. **93**, 1099 (2003).

[27] T. Kunikiyo, M. Takenaka, Y. Kamakura, M. Yamaji, H. Mizuno, M. Morifuji, K. Taniguchi, and C. Hamaguchi, A Monte Carlo simulation of anisotropic electron transport in silicon including full band structure and anisotropic impact-ionization model, J. Appl. Phys. **75**, 297 (1994).

[28] M. V. Fischetti and S. E. Laux, Monte Carlo analysis of electron transport in small semiconductor devices including band-structure and space-charge effects, Phys. Rev. B **38**, 9721 (1988).

[29] Y. Kamakura, R. Fujita, K. Konaga, Y. Ueoka, N. Mori, and T. Kotani, in *2016 International Conference on Simulation of Semiconductor Processes and Devices (SISPAD)* (IEEE, Nuremberg, Germany, 2016), p. 47.

[30] I. Prigozhin, S. Dominici, and E. Bellotti, FBMC3D – A large-scale 3-D Monte Carlo simulation tool for modern electronic devices, IEEE Trans. Electron Devices **68**, 279 (2020).

[31] M. Goano, E. Bellotti, E. Ghillino, G. Ghione, and K. F. Brennan, Band structure nonlocal pseudopotential calculation of the III-nitride wurtzite phase materials system. Part I. Binary compounds GaN, AlN, and InN, J. Appl. Phys. **88**, 6467 (2000).

[32] P. Giannozzi, S. Baroni, N. Bonini, M. Calandra, R. Car, C. Cavazzoni, D. Ceresoli, G. L. Chiarotti, M. Cococcioni, and I. Dabo, *et al.*, Quantum ESPRESSO: A modular and open-source software project for quantum simulations of materials, J. Phys.: Condens. Matter **21**, 395502 (2009).

[33] P. Giannozzi, O. Andreussi, T. Brumme, O. Bunau, M. B. Nardelli, M. Calandra, R. Car, C. Cavazzoni, D. Ceresoli, and M. Cococcioni, *et al.*, Advanced capabilities for materials modelling with Quantum ESPRESSO, J. Phys.: Condens. Matter **29**, 465901 (2017).

[34] D. Hamann, Optimized norm-conserving Vanderbilt pseudopotentials, Phys. Rev. B **88**, 085117 (2013).

[35] M. Schlipf and F. Gygi, Optimization algorithm for the generation of ONCV pseudopotentials, Comput. Phys. Commun. **196**, 36 (2015).

[36] J. Heyd, G. E. Scuseria, and M. Ernzerhof, Hybrid functionals based on a screened Coulomb potential, J. Chem. Phys. **118**, 8207 (2003).

[37] D. Evans, A. G. McGlynn, B. M. Towlson, M. Gunn, D. Jones, T. E. Jenkins, R. Winter, and N. R. Poolton, Determination of the optical band-gap energy of cubic and hexagonal boron nitride using luminescence excitation spectroscopy, J. Phys.: Condens. Matter **20**, 075233 (2008).

[38] O. C. Zienkiewicz, R. L. Taylor, and J. Z. Zhu, *The Finite Element Method: Its Basis and Fundamentals* (Butterworth Heinemann, Oxford, UK, 2005).

[39] N. Christensen and I. Gorczyca, Optical and structural properties of III-V nitrides under pressure, Phys. Rev. B **50**, 4397 (1994).

[40] X. Gonze and C. Lee, Dynamical matrices, Born effective charges, dielectric permittivity tensors, and interatomic force constants from density-functional perturbation theory, Phys. Rev. B **55**, 10355 (1997).

[41] S. Baroni, S. de Gironcoli, A. Dal Corso, and P. Giannozzi, Phonons and related crystal properties from density-functional perturbation theory, Rev. Mod. Phys. **73**, 515 (2001).

[42] J. P. Perdew, K. Burke, and M. Ernzerhof, Generalized Gradient Approximation Made Simple, Phys. Rev. Lett. **77**, 3865 (1996).

[43] C. Verdi and F. Giustino, Fröhlich Electron-Phonon Vertex from First Principles, Phys. Rev. Lett. **115**, 176401 (2015).

[44] S. Poncé, E. R. Margine, C. Verdi, and F. Giustino, EPW: Electron–phonon coupling, transport and superconducting properties using maximally localized Wannier functions, Comput. Phys. Commun. **209**, 116 (2016).

[45] G. Pizzi, V. Vitale, R. Arita, S. Blügel, F. Freimuth, G. Géranton, M. Gibertini, D. Gresch, C. Johnson, and T. Koretsune, *et al.*, Wannier90 as a community code: New features and applications, J. Phys.: Condens. Matter **32**, 165902 (2020).

[46] F. Giustino, M. L. Cohen, and S. G. Louie, Electron-phonon interaction using Wannier functions, Phys. Rev. B **76**, 165108 (2007).

[47] E. O. Kane, Electron scattering by pair production in silicon, Phys. Rev. **159**, 624 (1967).

[48] T. Kunikiyo, M. Takenaka, M. Morifuji, K. Taniguchi, and C. Hamaguchi, A model of impact ionization due to the primary hole in silicon for a full band Monte Carlo simulation, J. Appl. Phys. **79**, 7718 (1996).

[49] N. Sano and A. Yoshii, Impact-ionization theory consistent with a realistic band structure of silicon, Phys. Rev. B **45**, 4171 (1992).

[50] J. P. Walter and M. L. Cohen, Frequency- and wave-vector-dependent dielectric function for silicon, Phys. Rev. B **5**, 3101 (1972).

[51] M. Farahmand, C. Garetto, E. Bellotti, K. F. Brennan, M. Goano, E. Ghillino, G. Ghione, J. D. Albrecht, and P. P. Ruden, Monte Carlo simulation of electron transport in the III-nitride wurtzite phase materials system: Binaries and ternaries, IEEE Trans. Electron Devices **48**, 535 (2001).

[52] E. Bellotti and F. Bertazzi, A numerical study of carrier impact ionization in $Al_xGa_{1-x}N$, J. Appl. Phys. **111**, 103711 (2012).

[53] H. Umezawa, T. Matsumoto, and S.-I. Shikata, Diamond metal–semiconductor field-effect transistor with breakdown voltage over 1.5 kV, IEEE Electron Device Lett. **35**, 1112 (2014).

[54] A. Hiraiwa and H. Kawarada, Figure of merit of diamond power devices based on accurately estimated impact ionization processes, J. Appl. Phys. **114**, 034506 (2013).

[55] H. Childs, *et al.*, in *High Performance Visualization—Enabling Extreme-Scale Scientific Insight*, (CRC Press, October 2012), p. 357.

[56] D. Litvinov, C. A. Taylor II, and R. Clarke, Semiconducting cubic boron nitride, Diamond Relat. Mater. **7**, 360 (1998).

[57] F. L. Nouketcha, Y. Cui, A. Lelis, R. Green, C. Darmody, J. Schuster, and N. Goldsman, Investigation of wide- and ultrawide-bandgap semiconductors from impact-ionization coefficients, IEEE Trans. Electron Devices **67**, 3999 (2020).

[58] M. M. Hayat, W. L. Sargeant, and B. E. Saleh, Effect of dead space on gain and noise in Si and GaAs avalanche photodiodes, IEEE J. Quantum Electron. **28**, 1360 (1992).

[59] H. Wen and E. Bellotti, Rigorous theory of the radiative and gain characteristics of silicon and germanium lasing media, Phys. Rev. B **91**, 035307 (2015).

[60] J. Kim and M. V. Fischetti, Electronic band structure calculations for biaxially strained Si, Ge, and III–V semiconductors, J. Appl. Phys. **108**, 013710-1 (2010).

[61] K. Tomizawa, *Numerical Simulation of Submicron Semiconductor Devices* (Artech House, 1993).